The Astrophysical Journal, 844:76 (15pp), 2017 July 20 https://doi.org/10.3847/1538-4357/aa7aaa

Prospective Out-of-ecliptic White-light Imaging of Interplanetary Corotating Interaction Regions at Solar Maximum

Ming Xiong[1,2,3], Jackie A. Davies[4], Bo Li[5], Liping Yang[1,2], Ying D. Liu[1,3], Lidong Xia[5], Richard A. Harrison[4], Hayashi Keiji[1,6], and Huichao Li[1,3]
[1] State Key Laboratory of Space Weather, National Space Science Center, Chinese Academy of Sciences, Beijing, China; mxiong@spacweather.ac.cn
[2] HIT Institute of Space Science and Applied Technology, Shenzhen, China
[3] University of Chinese Academy of Sciences, Beijing, China
[4] RAL Space, STFC-Rutherford Appleton Laboratory, Harwell Campus, Didcot, UK
[5] Shandong Provincial Key Laboratory of Optical Astronomy and Solar-Terrestrial Environment, Institute of Space Sciences, Shandong University, Weihai, China
[6] Institute for Space-Earth Environmental Research (ISEE), Nagoya University, Japan
Received 2017 May 26; revised 2017 June 13; accepted 2017 June 14; published 2017 July 24

Abstract

Interplanetary corotating interaction regions (CIRs) can be remotely imaged in white light (WL), as demonstrated by the Solar Mass Ejection Imager (SMEI) on board the Coriolis spacecraft and Heliospheric Imagers (HIs) on board the twin *Solar TErrestrial RElations Observatory* (*STEREO*) spacecraft. The interplanetary WL intensity, due to Thomson scattering of incident sunlight by free electrons, is jointly determined by the 3D distribution of electron number density and line-of-sight (LOS) weighting factors of the Thomson-scattering geometry. The 2D radiance patterns of CIRs in WL sky maps look very different from different 3D viewpoints. Because of the in-ecliptic locations of both the *STEREO* and Coriolis spacecraft, the longitudinal dimension of interplanetary CIRs has, up to now, always been integrated in WL imagery. To synthesize the WL radiance patterns of CIRs from an out-of-ecliptic (OOE) vantage point, we perform forward magnetohydrodynamic modeling of the 3D inner heliosphere during Carrington Rotation CR1967 at solar maximum. The mixing effects associated with viewing 3D CIRs are significantly minimized from an OOE viewpoint. Our forward modeling results demonstrate that OOE WL imaging from a latitude greater than 60° can (1) enable the garden-hose spiral morphology of CIRs to be readily resolved, (2) enable multiple coexisting CIRs to be differentiated, and (3) enable the continuous tracing of any interplanetary CIR back toward its coronal source. In particular, an OOE view in WL can reveal where nascent CIRs are formed in the extended corona and how these CIRs develop in interplanetary space. Therefore, a panoramic view from a suite of wide-field WL imagers in a solar polar orbit would be invaluable in unambiguously resolving the large-scale longitudinal structure of CIRs in the 3D inner heliosphere.

Key words: magnetohydrodynamics (MHD) – methods: numerical – solar wind – Sun: corona – Sun: heliosphere

Supporting material: animations

1. Introduction

The Sun, solar-system planets, and interplanetary space can be viewed as key elements of an interconnected system: the heliosphere. The inner and outer boundaries of the heliosphere are generally defined by an Alfvén surface inside the outer solar corona (Schwadron et al. 2010) and the heliopause surrounded by the local interstellar medium (Holzer 1989; Suess 1990), respectively. The heliosphere inside 1 au (about 215 solar radii, R_s) is termed the inner heliosphere. Understanding the causal connections between the Sun and the inner heliosphere is of fundamental importance to space physics and space weather (e.g., Schrijver et al. 2015). As a result of coronal expansion, the heliosphere is permeated with the supersonic, magnetized solar wind emerging from the Sun (Parker 1958; Hundhausen 1972). At solar minimum, the solar wind is inherently bimodal (McComas et al. 2000), with low-speed streams tending to emanate from near the ecliptic, and high-speed streams tending toward higher latitudes. Stream interaction regions (SIRs) are spiral structures formed in the heliosphere as a result of compression between fast and slow streams. SIRs form where fast solar wind is emitted behind slow solar wind along the same solar radial direction from the rotating Sun. The compression region lies very close to the stream interface, on the slow-wind side. Those SIRs that exist over consecutive solar rotations are termed corotating interaction regions (CIRs) (Gosling et al. 1993; Jian et al. 2006). CIRs were first observed during the Mariner-2 flight to and past Venus in 1962 (Neugebauer & Snyder 1966, 1967). The occurrence of an interplanetary SIR/CIR is characterized in terms of its in situ particle and wave signatures (Borovsky & Denton 2010) by: (1) a gradual transition from slow ($\sim$300 km s^{-1}) to fast solar wind (500 $\sim$ 700 km s^{-1}); (2) a deflection of the flow around the stream interface; (3) a rapid increase in the ion specific entropy ($T_i/n^{2/3}$) at the stream interface; (4) the generation of a compression region in which plasma density, magnetic field, and Alfvén speed are enhanced. The fast stream, slow stream, and SIRs/CIRs constitute the ambient solar wind flow in the heliosphere. The ambient solar wind flow, though stable overall, is always locally disturbed by small-scale transients, such as waves/turbulence, puffs, microstreams, and mini-ejecta.

The full corona around the Sun and a large portion of the inner heliosphere can be, and as of this writing are being, routinely observed in Thomson-scattered white light (WL). These are referred to as coronal imaging and heliospheric imaging, respectively. A WL imager measures the integrated line-of-sight (LOS) electron density, independent of temperature. As viewed by an observer, the angle between the Sun and the LOS is called elongation ε. As WL radiance I of the

inner heliosphere decreases with heliocentric distance r roughly as $I \propto r^{-3}$ (Jackson et al. 2010; Xiong et al. 2013b), the difference in WL brightness between the Sun and a solar wind feature, such as a coronal mass ejection (CME), at large ε is many orders of magnitude. Large CMEs at $\varepsilon = 45°$ have WL intensities that are of 10^{-14} $B_{\odot}$ order (DeForest et al. 2011), where $B_{\odot}$ is the mean solar brightness. The principal challenge of heliospheric imaging is the accurate removal of the background, which is typically two to three orders of magnitude brighter than typical solar wind features. The detectability in WL of a solar wind feature is determined by its signal-to-noise ratio. The main background sources for a deep-space heliospheric imager are ascribed to stray light, zodiacal light, and the star field. Although bright, these background signals are, fortuitously, relatively stable (Leinert & Pitz 1989). Specifically, the stray light, zodiacal light, and star field are approximately stationary in the instrumental, heliospheric, and celestial frames, respectively (DeForest & Howard 2015). By successfully subtracting the background brightness, a WL sky map taken by a heliospheric imager can reveal solar wind plasma transients illuminated by direct sunlight. Instrument specifications for a heliospheric imager on board a deep-space spacecraft also require a careful design that takes into account the potential stray-light impact of the spacecraft bus, spacecraft appendages, and other instruments (Harrison et al. 2005; Eyles et al. 2009). Historic spaceborne WL imagers, imaging both at corona and heliospheric distances, include the zodiacal-light photometers (Leinert et al. 1981) onboard the Helios spacecraft, the Large Angle and Spectrometric COronagraph (LASCO; Brueckner et al. 1995) onboard the *Solar and Heliospheric Observatory* (*SOHO*), the Solar Mass Ejection Imager (SMEI; Eyles et al. 2003) onboard the Coriolis spacecraft, and the Sun Earth Connection Coronal and Heliospheric Investigation (SECCHI; Howard et al. 2008) onboard the *Solar-TErrestrial RElations Observatory* (*STEREO*; Kaiser et al. 2008). In particular, the SECCHI instrument suite consists of five telescopes covering a broad range of fields of view, starting at the solar surface and extending all the way to the interplanetary space between the Sun and Earth. These *STEREO*/SECCHI telescopes are: an extreme ultraviolet imager (EUVI: $1 \sim 1.7\,R_s$), two Lyot coronagraphs (COR1: $1.5 \sim 4\,R_s$ and COR2: $2.5 \sim 15\,R_s$), and two wide-field heliospheric imagers (HI-1: $15 \sim 84\,R_s$ and HI-2: $66 \sim 318\,R_s$; Eyles et al. 2009). The COR1 and COR2 have nested FOVs in visible light, and image the inner and outer corona from 1.4 to 15 R_s. The *STEREO*/COR1 and LASCO/C1 are respectively designed as refractive and reflective types of space-borne internally occulted coronagraphs. The optical axes of HI-1 and HI-2 lie in the ecliptic. The elongation coverage in the ecliptic is approximately 4° to 24° for HI-1 and 18.°7 to 88.°7 for HI-2. The HI-1 and HI-2 FOVs are around 20° × 20° and 70° × 70°, respectively. Imaging the corona and heliosphere via Thomson-scattered sunlight has proved crucial to understanding solar wind structures and transients.

WL signatures of solar wind transients, such as SIRs/CIRs and CMEs, result from Thomson scattering of sunlight by free electrons, and therefore depend on both viewing geometry and electron density (e.g., Howard & Tappin 2009; Xiong et al. 2013a). The detectability of a solar wind feature in WL is actually more limited by perspective and Field-Of-View (FOV) effects than by its location relative to the Thomson scattering sphere (Howard & DeForest 2012). Since the advent of *STEREO*, SIRs/CIRs and CMEs can be continuously tracked in WL, from the inner corona all the way out to 1 au and beyond (e.g., Harrison et al. 2008; DeForest et al. 2011). The interpretation of the leading edge of the radiance pattern of a CME in particular, especially at larger elongations, is fraught with ambiguity (Howard & Tappin 2009; Xiong et al. 2013a, 2013b). Because a CME occupies a significant three-dimensional (3D) volume, different parts of the CME will contribute to the radiance pattern imaged by observers situated at different heliocentric longitudes (Xiong et al. 2013a). Even for an observer located at a fixed longitude, a different part of the CME will contribute to the imaged radiance corresponding to the leading edge of the CMEs WL signatures at any given time. Various techniques have been developed that enable the propagation directions of SIRs/CIRs and CMEs to be inferred, and hence their de-projected spatial locations and speeds based on fitting their time-varying radiance patterns (e.g., Rouillard et al. 2008; Sheeley et al. 2008; Tappin & Howard 2009; Liu et al. 2010; Lugaz et al. 2010; Wood et al. 2010; Möstl et al. 2011; Davies et al. 2012; Liu et al. 2016). The determination of interplanetary CME kinematics, and propagation direction in particular, is still riddled with potential uncertainties (Howard & Tappin 2009; Davies et al. 2012; Howard & DeForest 2012; Xiong et al. 2013a, 2013b). Because the *STEREO* spacecrafts orbit within the ecliptic, the longitudinal dimension is integrated in *STEREO*/HI imagery. The structure of CIRs is such that they would be better imaged from an out-of-ecliptic (OOE) viewpoint. OOE imaging from, for example, a solar polar orbit would enable the ecliptic to be mapped on a large scale.

An injection of the spacecraft into a solar polar orbit is extremely difficult, in contrast to an in-ecliptic mission such as *STEREO*. Tremendous energy is needed for a spacecraft to escape from the ecliptic. The International Solar Polar Mission (ISPM) was proposed as an OOE mission in the 1970s (Marsden & Wenzel 1981). For ISPM, two spacecraft were to be built, one by the National Aeronautics and Space Administration (NASA) and the other by the European Space Agency (ESA). One would be sent over Jupiter, to provide the gravity assist needed to alter the spacecraft flight path, then under the Sun. The other would fly under Jupiter, then over the Sun. All of the solar imaging instruments of ISPM were to be accommodated on the NASA spacecraft. However, due to cutbacks, the NASA spacecraft was canceled in 1981. For the remaining ESA spacecraft, NASA provided a Radioisotope Thermoelectric Generator (RTG) and launch services. The ISPM was renamed Ulysses, due to the indirect and untried flight path. Ulysses, without any imaging instrumentation, was launched using a space shuttle in 1990 after a Jovian swing-by; it finally reached an orbital inclination of 80°. Ulysses is the only successful OOE mission to orbit the Sun, and has enabled study of the solar wind at almost all latitudes (Wenzel et al. 1992; Smith et al. 1995; McComas et al. 2000). The two milestone missions of the Parker Solar Probe (PSP) and Solar Orbiter (SolO) are scheduled for launch in 2018. PSP, which remains close to the ecliptic, will use repeated gravity assists from Venus to incrementally decrease its orbital perihelion, such that it will eventually perform multiple passes at and within 8.5 R_s of the Sun, thereby touching the outer corona. SolO will use multiple Venus flybys to reduce its perihelion to around 60 R_s but also to progressively increase its orbital

inclination to an ultimate value of 36° (Muller et al. 2013). SolO includes a plethora of imaging instrumentation, whereas the only imaging instrument on PSP is the Wide-field Imager for Solar Probe (WISPR; Vourlidas et al. 2016). Several other OOE mission concepts have been proposed in the past; like SolO, they also carry both in situ and remote sensing instrumentation, enabling them to image solar and interplanetary activities from a high-latitude perspective. These OOE mission concepts include Solar Polar Imager (SPI; Liewer et al. 2008), POLAR Investigation of the Sun (POLARIS; Appourchaux et al. 2009), Solar Polar ORbit Telescope (SPORT; Wu et al. 2011; Xiong et al. 2016), and InterHelioProbe (Kuznetsov et al. 2016). The SPI mission proposes the use of solar sail propulsion to reach a 0.48 au circular orbit around the Sun with an inclination of 75°. The SPORT mission proposes using the gravity assist of Jupiter to achieve an elliptic polar orbit around the Sun with an inclination of 62° and perihelion at 0.7 au. The InterHelioProbe proposes using gravity-assisted maneuvers at Venus to maximize its orbital inclination and transform into a Polar-Ecliptic Patrol (PEP) phase. The potential synergy between PSP, SolO, and any other potential OOE spacecraft would enable the simultaneous exploration of the corona and heliosphere in three dimensions, and facilitate major breakthroughs in our understanding of the coupling between the Sun and the inner heliosphere.

Numerical forward magnetohydrodynamic (MHD) modeling of the inner heliosphere is crucial in synthesizing the WL signatures of SIRs/CIRs and CMEs from the unprecedented OOE perspective, and hence in providing justification for the definition of any OOE mission, particularly in terms of the inclusion of a suite of wide-field WL imagers. In this paper, we numerically synthesize WL imaging of interplanetary CIRs at solar maximum from an OOE perspective. The forward MHD model and its numerical solutions are presented in Section 2. Section 3 describes the 3D density distribution of CIRs in the corona and heliosphere. The WL radiance patterns of CIRs viewed from both ecliptic and OOE perspectives are elaborated in Section 4. Section 5 presents a tradeoff between orbit inclination and payload weight. Finally, the importance and feasibility of WL imaging from an OOE vantage point are discussed in Section 6.

2. Forward Modeling Procedure of Thomson-Scattering White Light

Numerical forward MHD modeling is crucial for establishing a causal link between solar-interplanetary dynamics and observable WL signatures, and hence providing valuable guidance for the optimization of future WL imaging. To investigate observable radiance patterns of CIRs in WL, we use MHD modeling to synthesize the WL signatures that would be remotely imaged from a number of widely distributed viewpoints in the inner heliosphere.

A 3D solar-interplanetary MHD model, based on a numerical Conservation Element/Solution Element (CESE-MHD) scheme (Feng et al. 2007, 2010, 2015), is used to study the large-scale density structures of CIRs during Carrington Rotation CR1967, in 2000 September. Photospheric synoptic magnetograms are prescribed as the inner boundary to drive the time-dependent CESE-MHD model. The simulated quasi-steady state of global solar wind flows during CR1967 is in good overall agreement with in situ measurements from the OOE Ulysses spacecraft and other near-Earth spacecraft (Yang et al. 2012). The simulated 3D distribution of electron density is used to generate synthetic 2D WL images.

The radiance of incident sunlight scattered off free electrons in the heliosphere is governed by the Thomson scattering geometry and the distribution of electron number density. Specifically, the observed WL radiance I is the LOS z-distance integral of the local WL radiance i as $I = \int_0^\infty i\, dz = \int_0^\infty n\, z^2\, G\, dz$ (Howard & Tappin 2009; Xiong et al. 2013a). The degree of polarization p of the scattered sunlight is defined as $p = I_t/I_r$, where I_t and I_r are two orthogonal components of the total brightness I. The mathematical expressions for G, I_t, and I_r are given in Equations (1) and (2) of Xiong et al. (2013a). The Thomson scattering geometry is described by the scattering angle χ, as depicted in Figure 1 of Xiong et al. (2013a). Here, $\chi = 90°$ corresponds to perpendicular scattering, whose locus constitutes the so-called Thomson sphere. The Sun and observer lie at opposite ends of one diameter of the Thomson sphere. The dependence of the Thomson-scattering geometry factors (z^2G, z^2G_R, z^2G_T) on scattering angle $\chi^* = 90° - \chi$ is shown in Figure 1(b) for one particular LOS along an elongation $\varepsilon = 20\overset{\circ}{.}7$. The steady solar wind electron density n approximately varies with the heliocentric distance r as $n \propto r^{-2}$. At $\chi^* = 0$, along any LOS (i.e., on the Thomson sphere), the heliocentric distance is smallest (Figure 1(c)), and the electron density is largest (Figure 1(d)). Using the approximation $n \propto r^{-2}$, the LOS distribution of the local intensity components (i_t and i_r) and the elongation dependence of the total intensity (I^*, I_R^*, I_T^*) and its polarization (p) are calculated via Thomson-scattering theory and shown in Figures 1(a) and (e)–(h), respectively. Note that the calculated total intensity (I^*, I_R^*, I_T^*) is linearly scaled with elongation $0° < \varepsilon < 180°$, and this is used to normalize the ε-dependence WL radiance I in Figures 7 and 9. As shown in Figure 1(a), the peak in local radiance i is broadened over large angles from the Thomson surface $\chi^* = 0°$. This broadening of the i–χ^* profile becomes increasingly more significant with increasing elongation (Howard & Tappin 2009; Jackson et al. 2010; Xiong et al. 2013a). Although the efficiency of Thomson scattering depends on scattering angle, the total WL radiance I of the inner heliosphere decreases with heliocentric distance r, roughly according to the expression $I \propto r^{-3}$ (Jackson et al. 2010; Xiong et al. 2013b).

3. Three-dimensional Density Distribution of CIRs in the Corona and Heliosphere

Solar wind emanating from the rotating Sun fills the whole heliosphere and creates a spiral pattern of interplanetary magnetic field lines. As discussed previously, we use the numerical CESE-MHD model to simulate the complex interplanetary structures that were present during CR1967, whose 2D cross-sections are presented in Figure 2, whose 3D iso-surface volumes are presented in Figures 3 and 6. Figure 2 shows the distribution of both density n and speed v_r in the corona and heliosphere as a function of longitude and latitude (a)–(c), in the equatorial plane (d)–(f), and in the east–west meridian as viewed from Earth (g)–(i). Figures 3 and 6 illustrate the iso-contour surfaces of density n in the corona and heliosphere, respectively. For Figures 2(e), (h), and 6, the density n is scaled with an r^2 fall-off. With the r^2 correction, the normalized density $n \cdot r^2$ from 30 to 215 R_s approximately maintains the same scaling of solar wind features as they

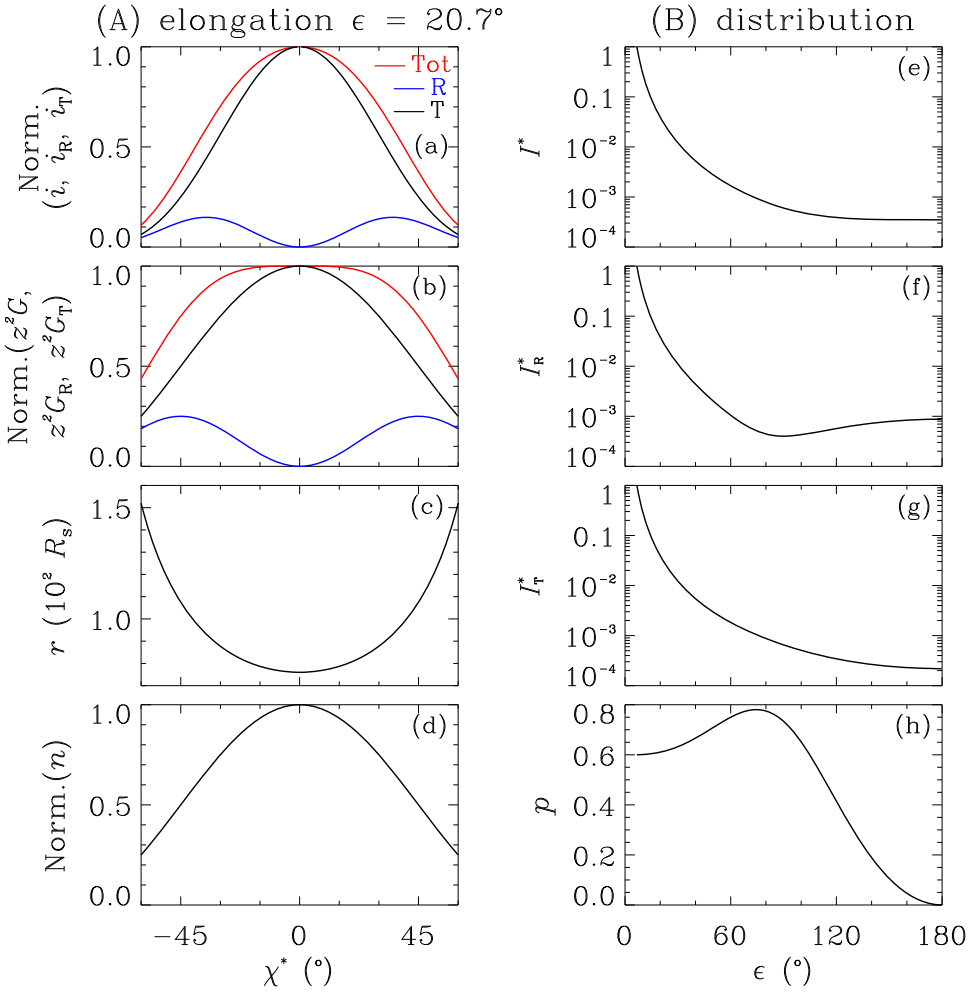

Figure 1. A reference factor I^* used to normalize the elongation ε dependence of WL brightness I. Assuming that $n \propto r^{-2}$, and using the known values of the Thomson-scattering geometry factors (z^2G, z^2G_R, z^2G_T), intensity profiles (i, i_R, i_T) calculated along one LOS at an elongation $\varepsilon = 20.^\circ7$ are presented in column (A). The LOS-integrated and linearly scaled intensities (I^*, I^*_R, I^*_T) over $0^\circ < \varepsilon < 180^\circ$ are presented in column (B). The polarization p derived from the intensities of I^*_R and I^*_T is given in panel (h).

propagate outward from the Sun. As the most conspicuous brightness feature in the corona, coronal streamers manifest as highly inclined ribbons on the solar source surface at 2.5 R_s (Figure 2(a)) and as multiple fan-like features emanating from the Sun in the equatorial and meridional cuts (Figures 2(d), (g)). Such bright emission from the streamers is ascribed to a confinement of dense plasma by closed magnetic field lines. On the photosphere underneath the coronal streamers lies a magnetic polarity inversion line (PIL; Zhao et al. 2005). As shown in Figure 2(a), the streamers astride the PIL reach heliographic latitudes as high as $\pm 60^\circ$; the polar coronal holes with low emission, due to their open magnetic field configuration, extend across the equator. A short-lived coronal hole also appears at low southern latitudes, near $\varphi = 90^\circ$. As noted in the introduction, at solar minimum, the stable solar wind configuration is bimodal, with fast streams from the polar coronal holes and slow streams near the equator. The fast solar wind (at a comparatively steady speed of about 700 km s^{-1}) emanates from large-scale regions of a single magnetic polarity in polar coronal holes (Smith et al. 1995; McComas et al. 2000; Cranmer 2002). The slow solar wind (300 $\sim$ 500 km s^{-1}), which emanates from magnetically complex regions at low latitudes and the periphery of coronal holes, permeates the ecliptic (Wang & Sheeley 1990; Li et al. 2004; Feldman et al. 2005). The balance between fast and slow solar winds is modulated by the 11 year solar cycle. At solar maximum, slow and fast streams occur at nearly all heliospheric latitudes (Figures 2(c), (i)). In regimes where fast solar wind is emitted behind slow solar wind, a CIR will form as a 3D spiral in interplanetary space that co-rotates with the Sun (Gosling & Pizzo 1999). Identified from its characteristic signatures in both density n (Figures 2(b), (e), (h)) and speed v_r (Figures 2(c), (f), (i)), an individual CIR manifests as a compression region at the interface of fast and slow streams. During CR1967, there are three CIRs in the ecliptic, each revealed as a spiral arm of density compression (Figure 2(e)). A CIR will have less azimuthal winding angle at higher latitudes θ, as the centrifugal speed of the solar wind away from the solar rotation axis is described by $v_r \cdot \cos\theta$. Broiles et al. (2012) find that (1) the mean azimuthal tilt of CIRs observed at 1 au agrees with what is predicted of the Parker spiral, while the mean meridional tilt is about 20°; (2) the meridional tilt of CIRs changes from one solar rotation to the next, with no relationship in its value between successive Carrington rotations. The large-scale 3D nature of CIR morphology numerically simulated in this paper is generally oversimplified as having a local planar geometry with both azimuthal and meridional tilts (e.g., Lee 2000).

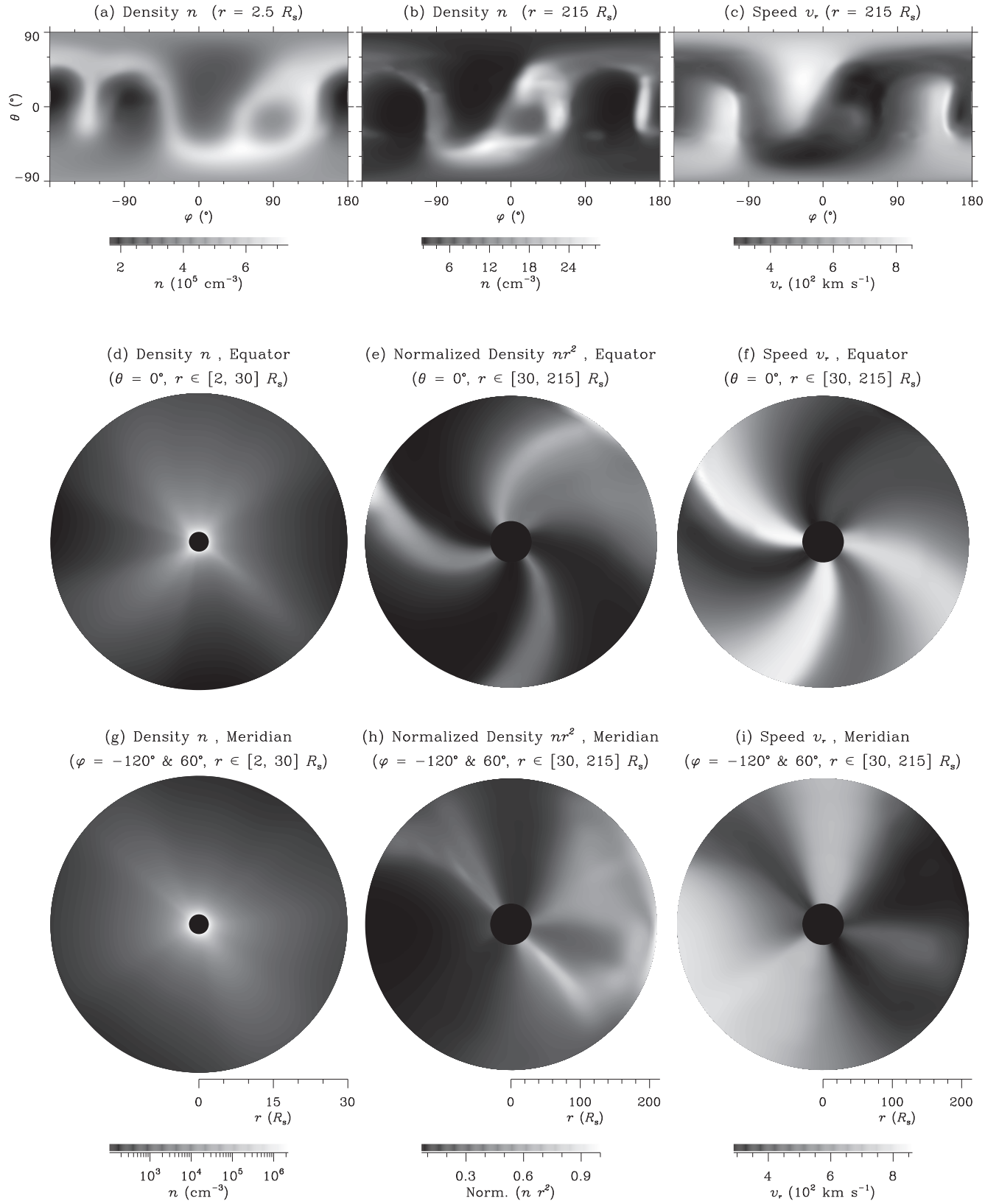

Figure 2. The distribution of proton density n and radial speed v_r of the ambient solar wind, at various radii (a)–(c), in the equator (d)–(f) and meridian (g)–(i) of the inner heliosphere in a 3D geometry of radius r, latitude θ, and longitude φ. Panels (a), (d), and (g) are at coronal altitudes; panels (b), (c), (e), (f), (h), and (i) are in the heliosphere. The interplanetary density, n, is normalized as $n \cdot r^2$ in panels (e) and (h).

The 3D morphology of corona streamers and interplanetary CIRs becomes increasingly more complex as the phase of the solar cycle increases from solar minimum to solar maximum. For CR1967, at solar maximum, the 3D iso-surfaces of modeled electron density in the corona and heliosphere are presented from the same perspectives in terms of $\theta_{\rm axis}$ and $\varphi_{\rm axis}$

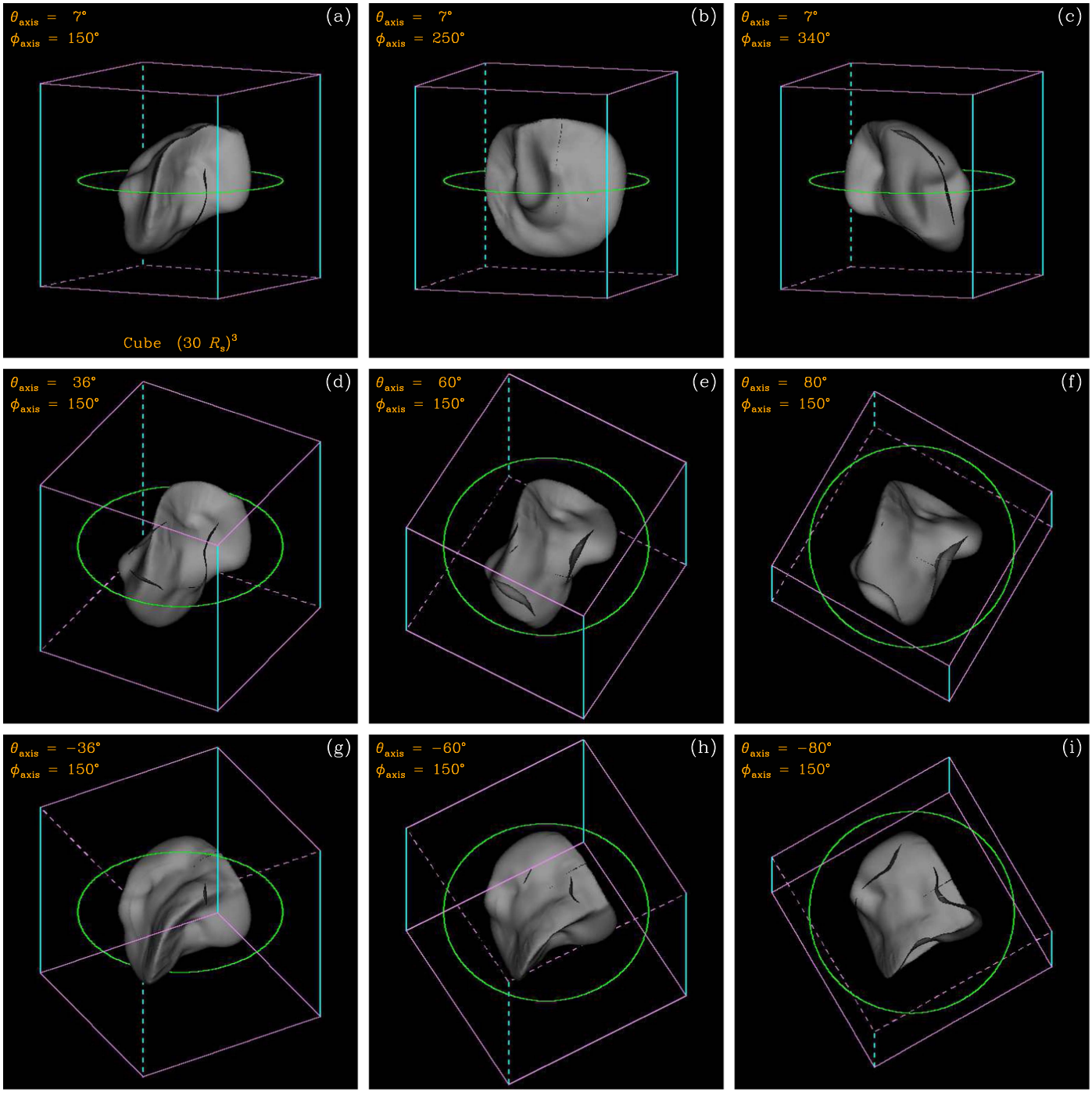

Figure 3. Three-dimensional iso-surfaces of coronal density n viewed from different vantage points. These vantage points, defined by $\theta_{\rm axis}$ and $\varphi_{\rm axis}$, are in or near the ecliptic for panels (a)–(c), at northern latitudes for panels (d)–(f), and at southern latitudes for panels (g)–(i). The circle corresponds to 30 $R_{\rm s}$ in the ecliptic. An animation of this figure is available to provide more perspectives of the 3D corona, both a latitudinal scan-view across the solar poles and a longitudinal scan-view near the ecliptic.

(An animation of this figure is available.)

in Figures 3 and 6. The subscript "axis" in $\theta_{\rm axis}$ and $\varphi_{\rm axis}$ refers to an LOS direction in the FOV center. The coronal streamer iso-surface is revealed as being highly irregular in Figure 3, significantly deviating from spherical symmetry around the Sun. Where the coronal plasma is confined within the streamers, it freely escapes beyond their bounds. The 3D morphology of a streamer is jointly determined by the magnetic PIL at the photosphere and pressure equilibrium across the streamer surface. Beyond the heliocentric distance of the cusp points of the very distorted coronal streamers (Figure 3), different solar wind flow regimes can interact and form highly warped CIRs in interplanetary space (Figure 6). Multiple CIRs coexist during CR1967, each extending over a large range of latitudes. A mixing effect associated with CIR imagery should be borne in mind when interpreting ambient large-scale solar wind features at solar maximum. When one front-side CIR overlaps with the other backside CIR from a viewer perspective, or when two and more CIRs are close together

but do not overlap, the mixing effect occurs. The mixing effect is most significant for observers near the ecliptic (Figures 6(a)–(c)), gradually reducing outside the ecliptic (Figures 6(d), (g)) until they almost disappear at heliospheric latitudes above 60° (Figures 6(e)–(i)). This latitude threshold of $\theta_{\rm axis} = \pm 60^\circ$ is confirmed from examining the location of coronal streamers in the synoptic density map of Figure 2(a), and applies to viewing CIRs in 3D throughout this solar cycle, because the observed magnetic PILs on the photosphere rarely protrude into the heliographic polar regions of $|\theta_{\rm PIL}| > 60^\circ$ even at a very strong solar maximum (Zhao et al. 2005). An observer above 60° latitude can resolve multiple CIRs and the complete spiral morphology of any CIR from the Sun to 1 au and beyond. The spiral morphologies of CIRs are clockwise (anti-clockwise) when viewed from northern (southern) latitudes. The mixing effect inherent when multiple CIRs coexist in 3D interfere with the study of CIRs from an ecliptic viewpoint, but can be significantly reduced by an OOE vantage point.

4. Two-dimensional Radiance Patterns of CIRs Viewed from an Out-of-Ecliptic Perspective

The electron density distribution between the Sun and the Earth can be imaged in WL from space. The WL intensity I of the inner heliosphere is proportional to a LOS integral of electron density, and, as discussed earlier, decreases with heliocentric distance r as $I \propto r^{-3}$. Mainly due to the design challenges imposed by the large dynamic range of WL intensity, the solar corona and interplanetary space are imaged separately, by coronagraphs and heliospheric imagers, respectively. Heliospheric imaging fills the large observation gap between near-Sun coronagraph imaging and in situ measurements (Eyles et al. 2009). In interplanetary space, the background solar wind speed is nearly constant and the background electron number density n_0 varies approximately with r^{-2}. However, the equilibrium defined by $n_0 \propto r^{-2}$ is disturbed by the presence of interplanetary transients such as CMEs and CIRs. The solar wind over a large portion of the inner heliosphere can be clearly imaged in Thomson-scattering WL, as has been most clearly demonstrated by the successful performance of the HI instruments on board the twin *STEREO* spacecraft. Here, we assume an ideal solar polar spacecraft (SPS) travelling in a 1 au circular orbit around the Sun, hypothesize that the spacecraft carries both a coronagraph and a heliospheric imager, and synthesize the WL emission of the corona and heliosphere from various perspectives. Our notional SPS must be a three-axis stabilized platform with sufficient pointing accuracy. Our assumed heliospheric imager is essentially an extremely wide-field coronagraph, following the overall optical design of the externally occulted *SOHO*/LASCO/C2 and C3 (Brueckner et al. 1995) and *STEREO*/COR2 (Howard et al. 2008) coronagraphs. Thus, the optical axis of the heliospheric imager on board SPS points toward the Sun, whereas that of the *STEREO*/HI points off the Sun-spacecraft line. In essence, we assume complete position angle coverage, which is not the case with *STEREO*/HI, but was the case with Coriolis/SMEI. In contrast to *STEREO*/HI, the technical difficulty of reducing the stray-light is a much greater challenge for the heliospheric imager on board SPS. The assumed plane-of-sky (POS) coverage of the FOV of the coronagraph and heliospheric imager on our idealized SPS is 2 to 30 R_s and 30 to 215 R_s, respectively, as the hosting SPS orbits at a constant heliocentric distance of 1 au.

The 2D WL radiance patterns of 3D CIRs are jointly determined by the electron density distribution and viewing perspective. Using the forward MHD modeling of the ambient solar wind during CR1967, we synthesize the WL emission from the corona (Figures 4, 5) and heliosphere (Figures 7, 8), as viewed from multiple perspectives by SPS. Total WL brightness I (Figures 4, 7) and polarization degree p (Figures 5, 8) are synthesized. The radial component of the 2D coordinate system used in Figures 4–8 is in units of elongation rather than heliocentric distance. The Thomson-scattering geometry effect can be effectively ignored in the corona, so the coronal emission is predominantly contributed by electrons in the POS of the observer. The POS cross-section of the 3D iso-surface of the coronal density distribution in Figure 3 is in good agreement with the radiance pattern of coronal streamers in Figure 4. The density ridge corresponding to the presence of coronal streamers in Figure 3 is sharp and irregular, because of the meandering of the underlying photospheric magnetic PIL at solar maximum. Only the near-POS section of this density ridge is observed by the coronagraph, resulting in one protruding brightness feature in Figure 4. The degree of polarization p, presented in Figure 5 from the same perspectives, indicates the spatial location of the radiance patterns shown in Figure 4. At solar maximum, there are multiple coronal streamers, distributed over both high and low heliographic latitudes. Thus, a coronagraph located at any vantage point can readily image at least one streamer. The global distribution of coronal density is shaped by the photospheric distribution of positive and negative magnetic flux. Coronal density structures co-rotate almost rigidly with the Sun. Although the solar rotation Ω plays little part in shaping the structure of coronal streamer, it can significantly affect the large-scale morphology of interplanetary CIRs. CIRs, which form at the interface between fast and slow solar wind flow, gradually develop into a leading compression region followed by a rarefied region at large heliocentric distances, and then ultimately evolve into a forward-and-reverse fast shock pair beyond 1 au (Gosling 1996). In particular, at solar maximum, CIRs are highly warped and distorted from a simple spiral form (Figure 6). That spiral morphology of CIRs is not, however, directly observable from imagers in the ecliptic (Figures 7(a)–(c)). The ecliptic vantage point of all WL coronal and heliospheric imagers, to date, has led to the integration of that longitudinal dimension. A WL imager in a solar polar orbit would provide the first-ever images of both the solar polar regions and the ecliptic from an OOE viewpoint. As demonstrated in Figures 7(d)–(i), an OOE imager could have a panoramic view of the ecliptic, unambiguously resolve the longitudinal structure of CIRs, and enable the continuous tracking of the CIRs from the Sun to 1 au.

The radiance patterns of 3D CIRs are different when viewed from different perspectives. From an ecliptic vantage point, the radiance patterns of CIRs manifest as bubble fronts, angular fans, and ray bundles. Such a complicated mixture of different patterns, as seen in Figures 7(a)–(c), is ascribed to the mixing effect resulting from the co-existence of multiple CIRs (see Figures 6(a)–(c)), as discussed in Section 3. When viewed from an OOE viewpoint, these effects are minimized such that the radiance pattern of each CIR can be clearly distinguished as a distinct, well-separated, spiral (Figures 7(d)–(i)). Moreover, in contrast to an ecliptic view, the radiance patterns from an OOE view are more extensive and brighter in intensity. For a WL imager at different latitudes $\theta_{s/c}$ and the same longitude $\phi_{s/c}$

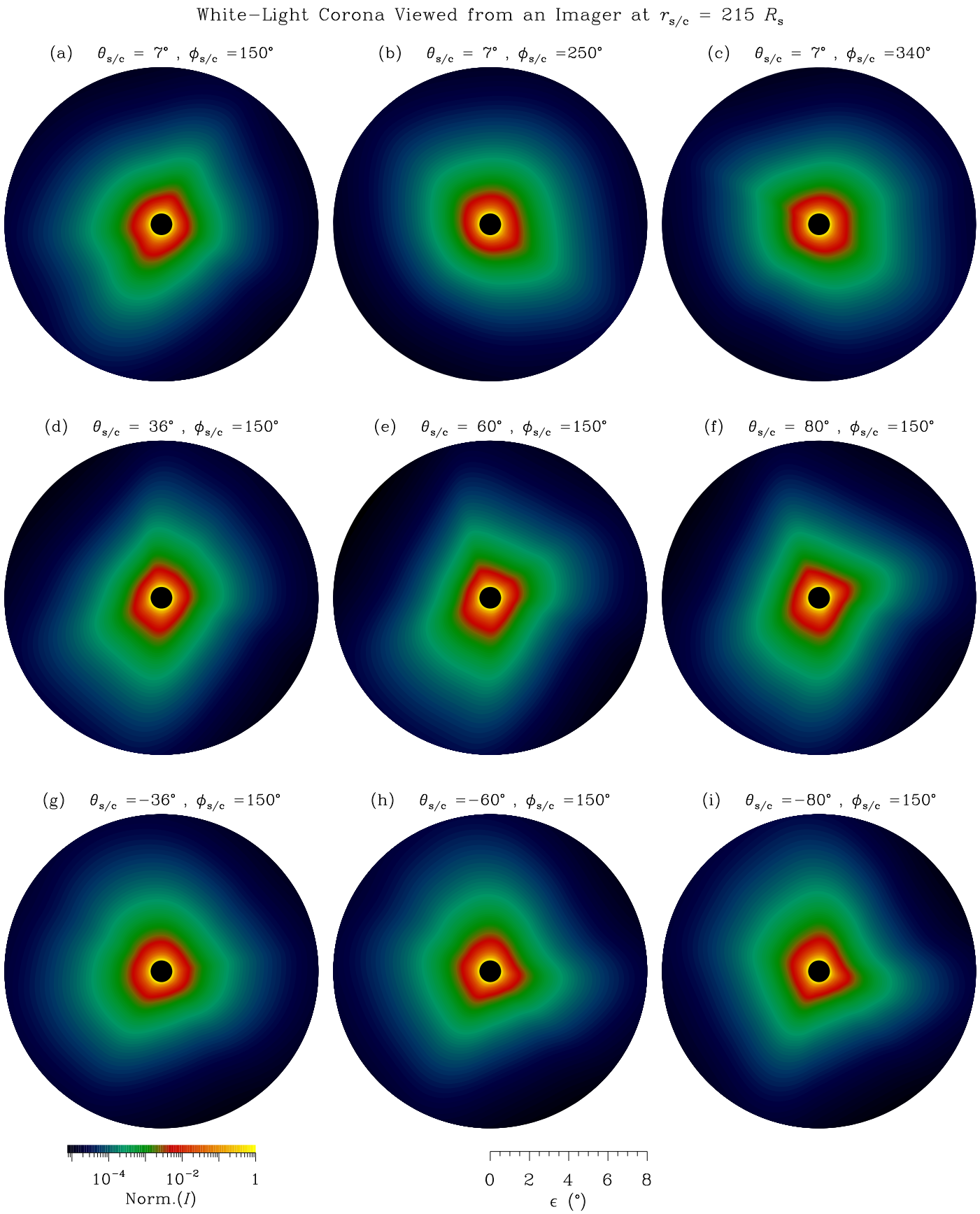

Figure 4. The WL brightness I of the corona in the elongation range $\varepsilon \in [0.^{\circ}5, 8^{\circ}]$, theoretically calculated from various $\theta_{s/c} - \varphi_{s/c}$ viewpoints as prescribed in Figure 3. This elongation range corresponds to a distance range of [2, 30] R_s in the plane-of-sky.

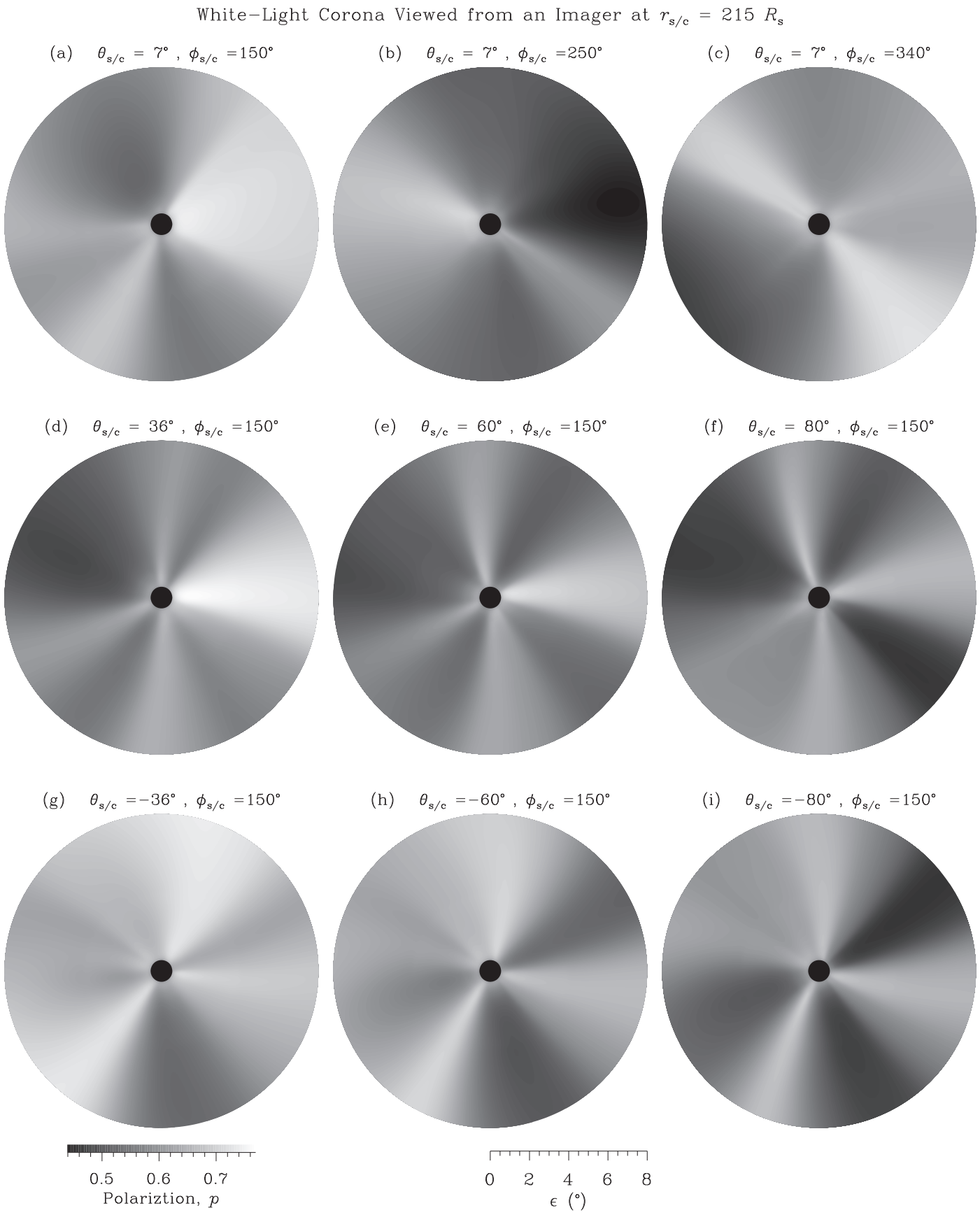

Figure 5. The degree of polarization p of WL emission from the corona, as observed from the perspectives prescribed in Figure 3.

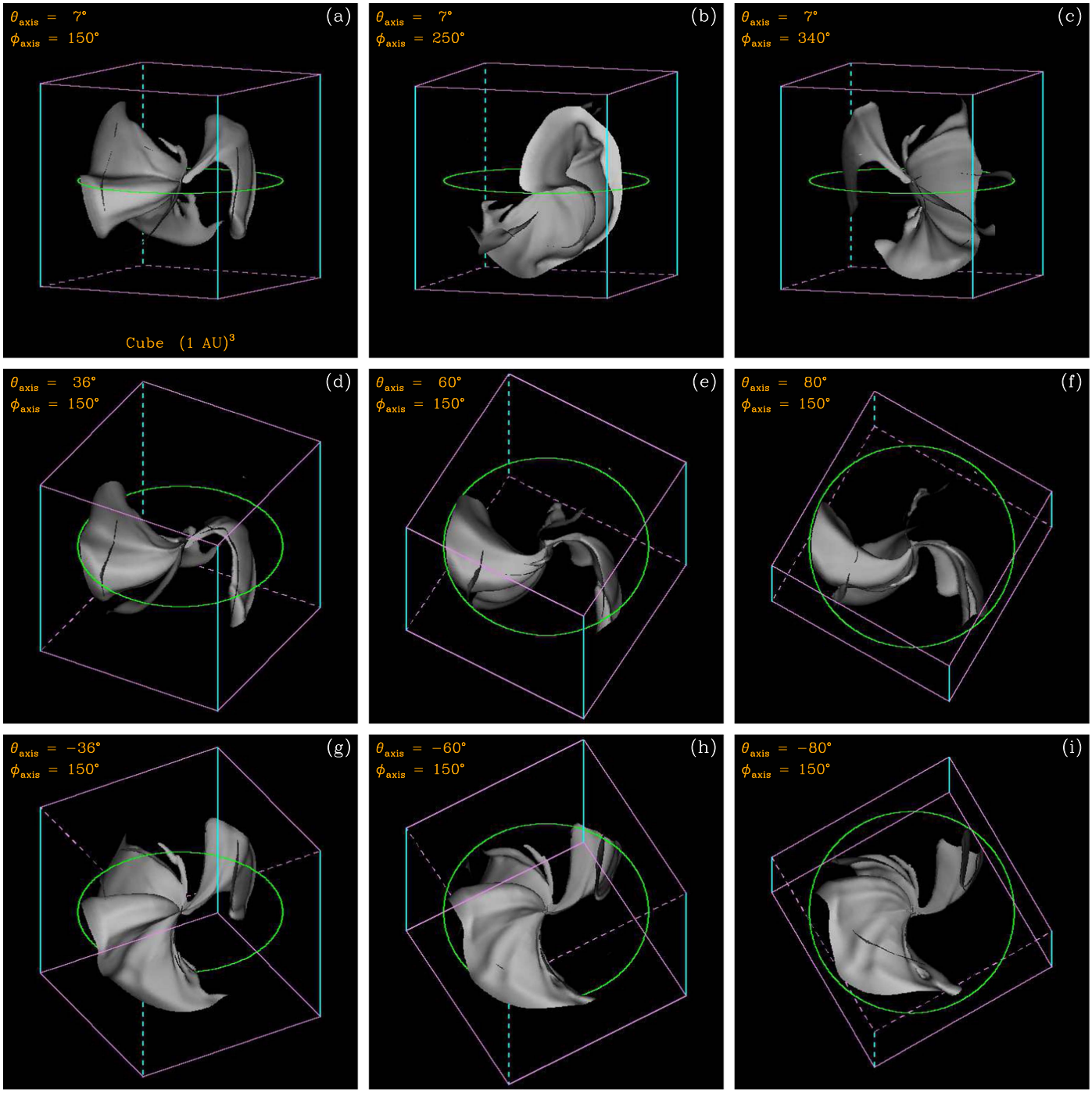

Figure 6. A 3D iso-surface of the normalized interplanetary density $n \cdot r^2$ viewed at different angles. The circle corresponds to 1 au in the ecliptic. An animation is available to provide more perspectives of the 3D heliosphere; both a latitudinal scan-view across the solar poles and a longitudinal scan-view near the ecliptic.

(An animation of this figure is available.)

$= 150°$, the total radiance I along a fixed elongation $\varepsilon = 20.^{\circ}7$ is presented in Figure 9 as a function of azimuthal angle φ.

The local minimum in I that is evident at $\varphi = 200°$ for $\theta_{s/c} = 7°$ (corresponding to an ecliptic vantage point), is less pronounced at $\varphi = 225°$ for $\theta_{s/c} = 36°$, and all but disappears for $\theta_{s/c} = 60°$. This local minimum and the peak in I directly to its right are depicted as a star and a solid dot, respectively, in Figures 9, 7(a), (d), (e). The gradual disappearance of this "low emission zone" that accompanies the increasing in spacecraft latitude from 7° via 36° to 60° is evident from examination of Figures 7(a), (d), and (e). At latitudes above 60°, the spiral morphology and brightness of the observed CIRs evolve little and remain relatively unchanged (cf., Figures 7(e)–(i)). The WL intensity of interplanetary CIRs is the LOS integral of electron number density, weighted by the Thomson-scattering geometry factor (Figure 1). For the six typical LOSs corresponding to the stars and solid dots in Figures 7 and 9, the LOS density profiles as a function of scattering angle χ^* are

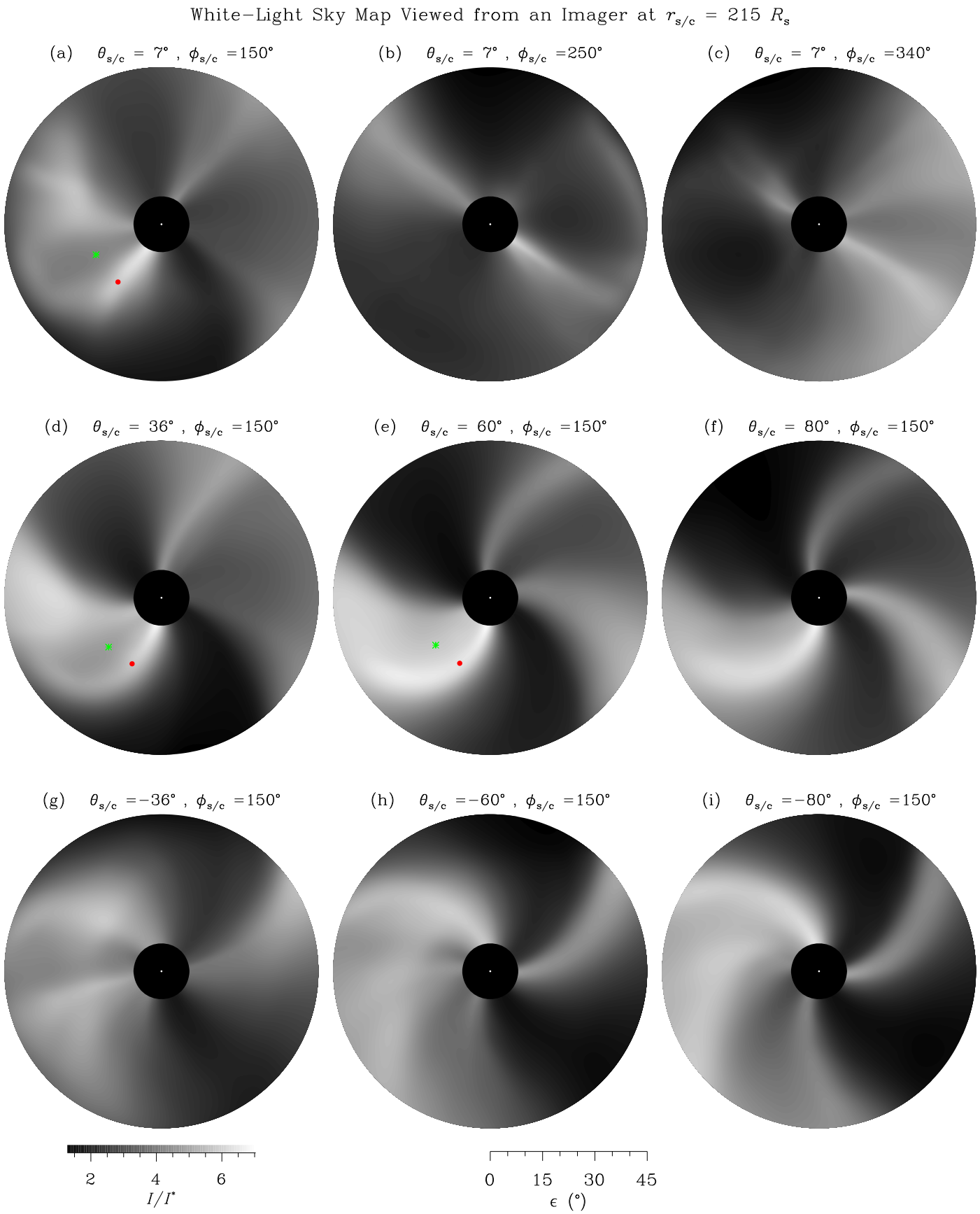

Figure 7. The normalized WL brightness I/I^* of the interplanetary medium over the elongation $\varepsilon \in [8°, 45°]$ is theoretically calculated from various 3D viewpoints in terms of $\theta_{s/c}$ and $\varphi_{s/c}$ as prescribed in Figure 6. The concentric black and white circles in panels (a)–(i) correspond to the inner elongation and the solar-disk size, respectively. The dots and asterisks in Figures 7(a), (d), (e), and 9(a)–(c) have six LOS correspondences in terms of $\theta_{s/c}$, $\varphi_{s/c}$, and ε.

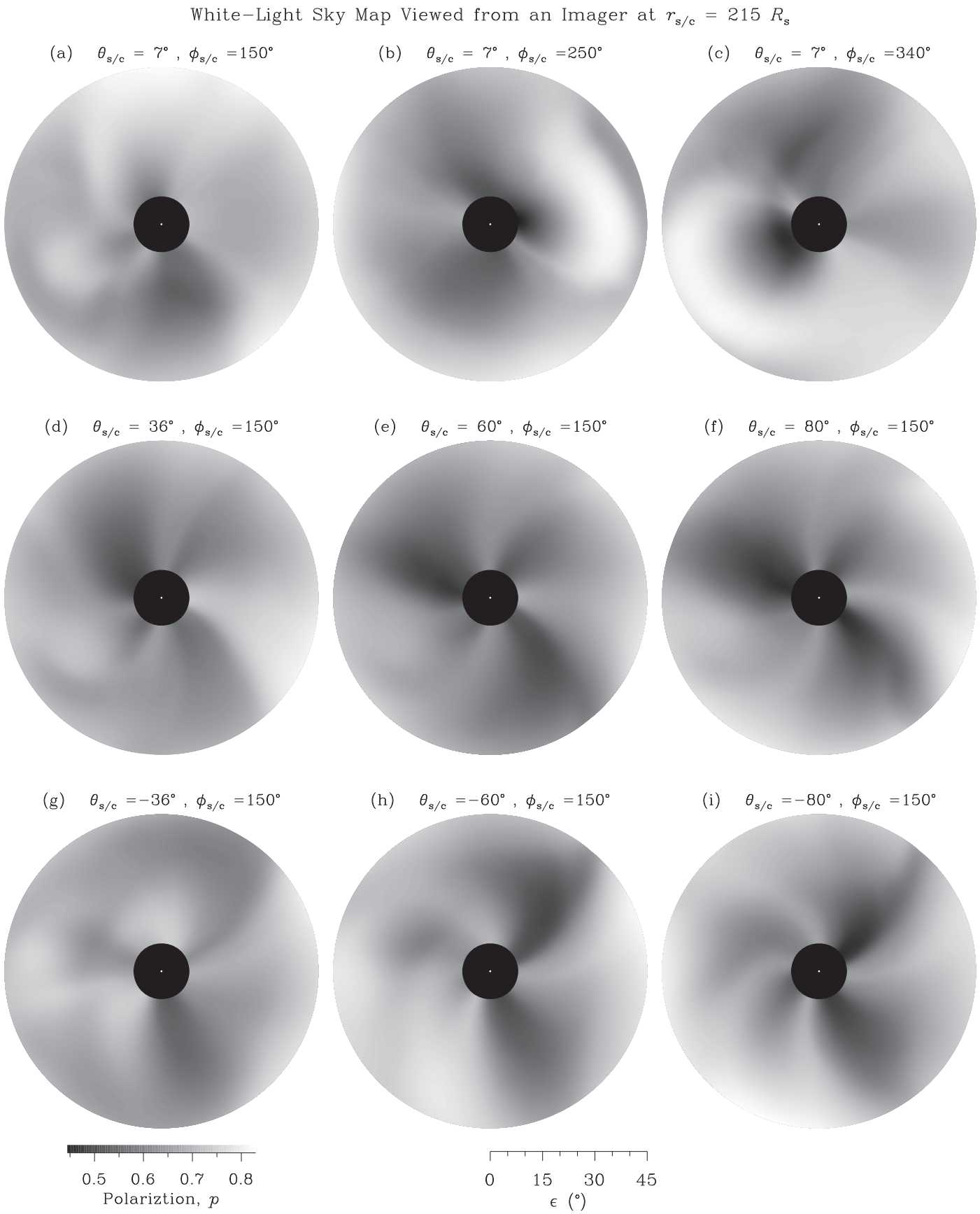

Figure 8. The degree of polarization p of interplanetary emission in WL, as observed from the perspectives prescribed in Figure 6.

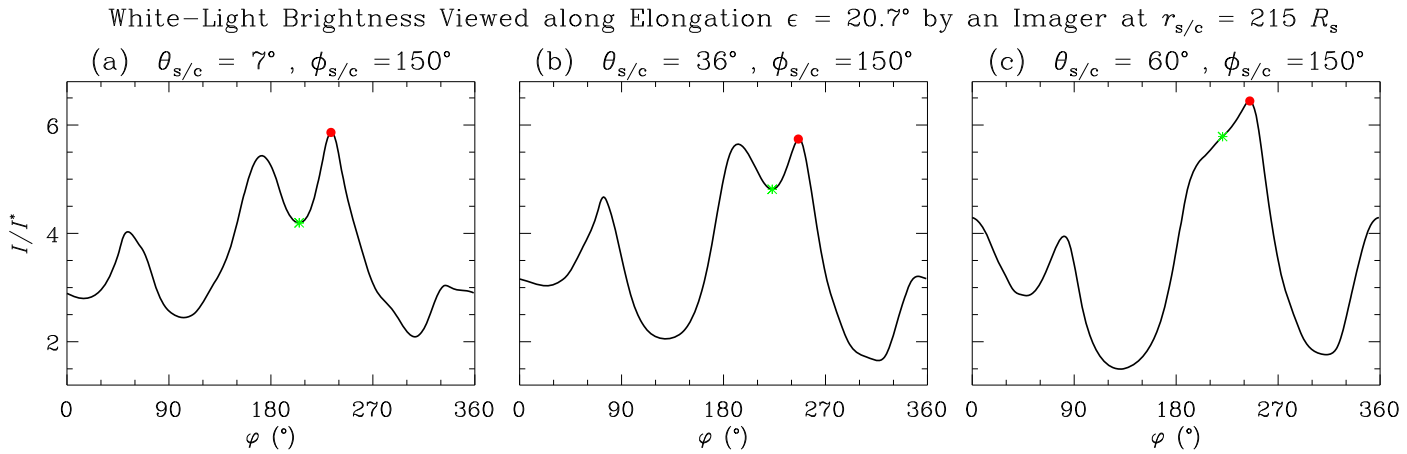

Figure 9. WL interplanetary brightness viewed along elongation $\varepsilon = 20.^{\circ}7$ from a heliocentric distance of 1 au. The dots and asterisks in panels (a)–(c) correspond to the LOSs in the WL sky map in Figures 7(a), (d), and (e).

shown in Figure 10. For the ecliptic LOS, denoted as a dashed line in Figure 10(a), it can be seen that the aforementioned weak emission is caused by two factors: (1) the offset of the density peak from $\chi^* = 0^\circ$, (2) the narrow Full Width at Half Maximum (FWHM) of the density peak. In contrast to the ecliptic viewpoint, the Thomson sphere from an OOE viewpoint always cuts across the compression region of a CIR (Figures 10(b), (c)). A CIR can be characterized as a warped 3D layer of finite thickness, being compressed in the longitudinal dimension and extended in the latitudinal dimension. As a result, an LOS from an ecliptic viewpoint will tend to cross a much narrower segment of the CIR than is crossed by an LOS from an OOE viewpoint (Figures 6, 7, 10). Moreover, an LOS from an ecliptic observer may penetrate through two or more coexisting CIRs, even if those CIRs are separated by tens of degree. An LOS from an OOE observer always intersects only a single CIR, even if multiple CIRs coexist at solar maximum. An LOS from an OOE observer at 60° latitude (Figure 10(c)) intersects an extended portion of the high-density compression zone near the Thomson-scattering sphere. OOE views are very favorable for imaging the complete CIR structure from the corona all the way to 1 au. Interplanetary CIRs are generally identified in *STEREO*/HI and SMEI data on the basis of their characteristic spatio-temporal radiance signatures in time-elongation maps, commonly called J-maps (e.g., Rouillard et al. 2008; Sheeley et al. 2008; Davies et al. 2012; Harrison et al. 2012; Xiong et al. 2013a). SIR/CIRs have significant longitudinal variability associated with the intermittent release, and subsequent entrainment and compression, of small-scale solar wind transients at the stream interface (Wang et al. 1998; Rouillard et al. 2008; Sheeley et al. 2008; Chen et al. 2009). It is by means of detecting these small-scale transients, and in particular, observing the characteristic patterns that they form in J-maps, that the presence of CIRs are most clearly inferred in heliospheric imagery (Rouillard et al. 2009). However, the use of J-Maps for the identification of CIRs is difficult under the following conditions (Plotnikov et al. 2016): (1) when multiple CIRs are present in the FOV at the same time; (2) when multiple CMEs pass through the FOV at the same time as the passage of the CIR. Using J-maps to analyze CIRs in heliospheric imagery at solar maximum is extremely challenging. The complex structuring of the corona and heliosphere at solar maximum is affected by the size and distribution of coronal holes, and the position and shape of coronal streamer belts. As a CIR is viewed at larger elongations, its associated WL signatures become fainter. Owing to Thomson scattering geometry effects, the kinematic properties of interplanetary CIRs inferred from ecliptic perspectives become increasingly ambiguous with increasing large elongations. However, the ambiguities that arise due to the Thomson-scattering geometry can be reduced from an OOE perspective. Additional WL polarization measurements can further limit the ambiguity of localizing CIRs. WL polarization has, up until now, only been measured in the corona (e.g., Moran & Davila 2004; Pizzo & Biesecker 2004; de Koning et al. 2009). WL polarization measurements in interplanetary space have, in the past, been numerically investigated in terms of their potential merit in the localization of CMEs along the LOS (Xiong et al. 2013b). Simulated polarization images of interplanetary CIRs during CR1967 are presented in Figure 8. Polarized imaging potentially allows for the accurate localization in interplanetary space of CMEs and CIRs in 3D from a single vantage point. Thus, a polarizing heliospheric imager is widely touted as being a critical next-generation tool for space weather monitoring and prediction (e.g., DeForest et al. 2016). Owing to a heritage extending back over more than 40 years, most notably by SMEI (Eyles et al. 2003) and *STEREO*/HI (Eyles et al. 2009), interplanetary imaging of total WL brightness is feasible at a high technology readiness level. As demonstrated by the synthesized total-brightness images presented in Figure 7, panoramic WL imaging from an OOE vantage point enables multiple CIRs simultaneously present within the FOV to be easily resolved, solar wind flow within each CIR to be continuously traced out to 1 au, and the spatial curvature of each CIR to be readily identified.

5. Tradeoff between Orbit Inclination and Payload Weight

A potential OOE spacecraft mission with multi-wavelength imaging capability would revolutionize our understanding of the structure and dynamics of the Sun–Earth system. It is difficult to inject an OOE spacecraft into a solar polar orbit, because tremendous energy is needed for the spacecraft to escape from the ecliptic. The tradeoff between the inclination of a spacecraft in a solar polar orbit and its payload mass has to be considered in terms of a cost-benefit analysis. Any risks in terms of the instruments, platform, and rocket should be minimized at a high technology readiness level. Design of the orbit is crucial to enable the scientific objectives of a

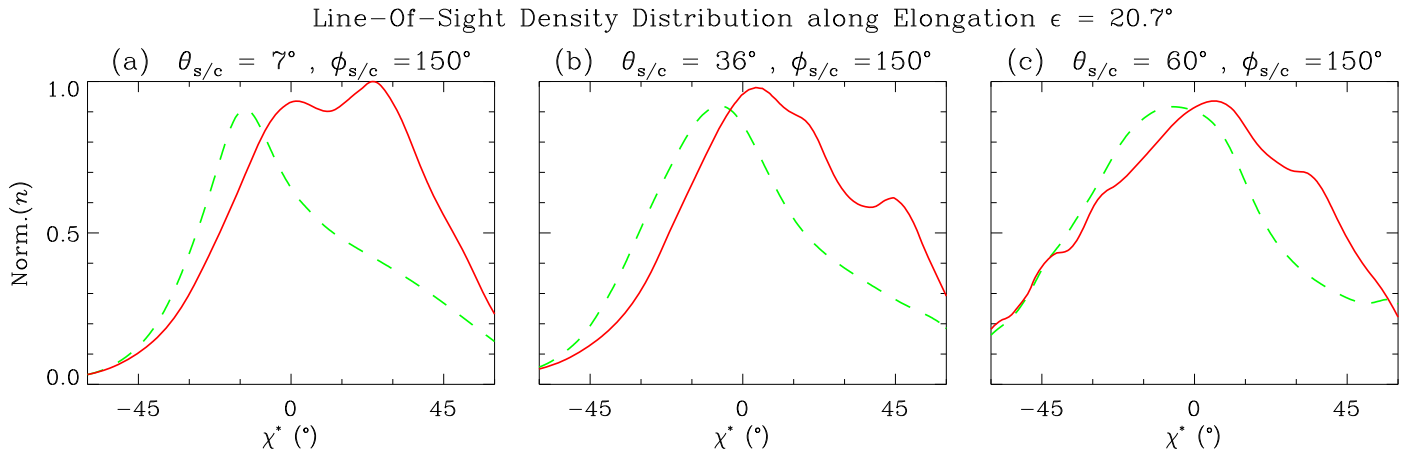

Figure 10. Distribution of normalized density Norm.(n) along a modified scattering angle χ^* for six LOS. These LOS are from the same solar elongation $\varepsilon = 20.^{\circ}7$ and different latitudinal perspectives $\theta_{s/c}$ = [7°, 36°, 60°]. The solid and dashed lines in panels (a)–(c) correspond to the dot-denoted and asterisk-denoted LOS in Figures 7(a), (d), and (e).

heliospheric satellite mission to be successfully achieved. The most critical parameter of any solar polar orbit is the OOE inclination angle. Other factors, such as the launch vehicle, launch time window, and gravity assist must also be considered in the orbit design. The capability of the launcher and the weight of the payload significantly restrict the inclination angle.

The OOE maneuvers of future deep-space satellites can be powered by planetary gravity assists or solar sail propulsion. The historic Ulysses spacecraft had a mass of 370 kg, a power of 285 W, and an orbital inclination of 80° achieved with a gravity assist from Jupiter (Wenzel et al. 1992). The imminent SolO mission will, it is believed, reach an inclination angle of 36°, using multiple Venus flybys (Muller et al. 2013). Other proposed OOE mission concepts include SPI (Liewer et al. 2008), POLARIS (Appourchaux et al. 2009), SPORT (Wu et al. 2011; Xiong et al. 2016), and InterHelio-Probe (Kuznetsov et al. 2016). To escape from the ecliptic, SPORT and SPI use a Jupiter flyby and solar sail, respectively. After entering a large elliptical transfer orbit heading toward Jupiter, it is designed that a Jovian swing-by will inject SPORT into an elliptical polar orbit around the Sun with an inclination angle of 62°, a perihelion and aphelion of 0.7 and 5 au, respectively, and an orbital period of five years. Imaging observations of the Sun and interplanetary space will commence when SPORT is within 2 au of the Sun. Hence, out of an orbit of five years, SPORT will take images for almost nine months. In order to prolong the imaging observation time, the use of further multiple gravity assists from Venus or Earth have been explored to reduce the aphelion of the OOE orbit toward 2 au. These orbital maneuvers will also increase the inclination angle to nearer 70°. Using an additional Venus (Earth) swing-by would extend the imaging observation time 25 (31) months during the designed SPORT lifetime of 10 years (Xiong et al. 2016). In contrast to SPORT, SPI intends to use solar sail technology to achieve its OOE orbit. This technology is currently being demonstrated in space by the IKAROS (Interplanetary Kite-craft Accelerated by Radiation Of the Sun) mission. The circular orbit of SPI is prescribed as having a radius of 0.48 au, inclination angle of 75°, and orbital period of four months. Both SPI and SPORT are proposed to carry a suite of in situ and remote-sensing instrumentation, thus enabling studies of the causal link between the Sun, the solar wind, and geospace. According to the forward modeling results presented in this paper, an inclination angle of $\theta_{s/c} \geqslant 60^{\circ}$ would offer significant benefits in the study of the background solar wind, and CIRs in particular. Lessons in how to optimize a future solar polar orbiting mission should be learned from Ulysses (Wenzel et al. 1992) and the forthcoming SolO (Muller et al. 2013). In contrast to SPI and SPORT, Ulysses flew without any remote-imaging instruments. A WL imaging suite including one or more coronagraphs and heliospheric imagers would be an invaluable component of the scientific payload on board any OOE spacecraft. The utility of the latter, in particular, is confirmed by the fact that a heliospheric imager is the only remote-sensing instrument on the upcoming PSP mission (Vourlidas et al. 2016).

The operating and forthcoming spacecraft missions (i.e., Solar Dynamics Observatory (SDO), *Advanced Composition Explorer* (*ACE*), WIND, PSP, and SolO) as well as other potential OOE and Lagrangian-5 missions should be coordinated within the International Living With a Star (ILWS) framework for the purpose of coordinated exploitation of the inner heliosphere. In particular, a wide-field WL heliospheric imager on board an OOE spacecraft at latitudes $\theta_{s/c} \geqslant 60^{\circ}$ could have an FOV that encompassed the orbits of PSP and SolO, which would provide a crucial contextual link for in situ and remote-sensing instruments on board these other spacecraft at low and intermediate latitudes. Coordinated observations from PSP, SolO, and other potential OOE missions could provide a unique scientific asset with which to study the inner heliosphere in 3D and reveal how solar activity drives heliospheric variability.

6. Discussion and Summary

In this paper, we conduct a data-driven numerical MHD simulation of interplanetary CIRs, and synthesize their WL emission on the basis of Thomson-scattering theory (e.g., Billings 1966; Howard & Tappin 2009; Xiong et al. 2013a). WL imaging is a mainstream technology for remotely sensing the corona and heliosphere. To date, all previous WL observations have been made from within the ecliptic; the only OOE spacecraft, Ulysses, did not host any imaging instruments (Wenzel et al. 1992). Hence, the longitudinal dimension of CIRs and CMEs has, up to now, been far integrated by all observations. The forthcoming SolO, to be launched in 2018, will cruise at an eccentric orbit as close as 60

R_s, reach a latitudinal inclination of 36°, and image the Sun from a closest-ever distance (Muller et al. 2013). Some other OOE mission concepts have been proposed, such as SPI (Liewer et al. 2008), SPORT (Wu et al. 2011; Xiong et al. 2016), and InterHelioProbe (Kuznetsov et al. 2016). Figure 6 shows that realistic CIRs have a complicated morphology in 3D. As demonstrated in the proof-of-concept study presented here, an OOE view from high latitudes can unambiguously resolve the large-scale spiral features of CIRs in the longitudinal dimension. An OOE imager has a more favorable Thomson-scattering geometry to collect photons scattered from interplanetary CIRs. Because of more favorable Thomson-scattering geometry, the WL emission of CIRs is usually brighter in the FOV of an OOE imager than in that of an ecliptic imager. A WL imager at high latitudes can have FOV that can encompass the ecliptic-orbiting spacecraft, which is crucial to provide a contextual link for in situ and remote-sensing observations.

In closing, a panoramic OOE view from WL imagers in a solar polar orbit is crucial to unambiguously resolve the large-scale structures of CIRs in the longitudinal dimension of the 3D inner heliosphere. The ambiguities that arise due to the Thomson-scattering geometry can be significantly minimized from an OOE vantage point. Heliospheric imaging instruments and their post-processing algorithms should be considered as unified systems (DeForest et al. 2011; DeForest & Howard 2015). Moreover, it should be realized that numerical MHD simulation driven by solar disk observations are very beneficial in interpreting the WL radiance patterns of coronal and interplanetary transients, establishing the requirements of future spaceborne WL imagers, and validating numerical modeling of the corona and heliosphere.

This work is jointly supported by the National Natural Science Foundation of China (41374175, 41231068, 41531073, 41627806, 41274176, 41474149, and 41674172), the Specialized Research Fund for State Key Laboratories of China, and the Strategic Priority Research Program on Space Science from the Chinese Academy of Sciences (XDA04060801). Jackie A Davies and Richard A Harrison are funded by the European Union Seventh Framework Programme (FP7/2007-2013) under grant agreement No. 606692 (HELCATS). We sincerely thank the anonymous referee for helpful suggestions.

References

Appourchaux, T., Liewer, P., Watt, M., et al. 2009, ExA, 23, 1079
Billings, D. E. 1966, A Guide to the Solar Corona (San Diego, CA: Academic)
Borovsky, J., & Denton, M. 2010, JGRA, 115, 10101
Broiles, T. W., Desai, M. I., & McComas, D. J. 2012, JGR, 117, A03102
Brueckner, G. E., Howard, R. A., Koomen, M. J., et al. 1995, SoPh, 162, 357
Chen, Y., Li, X., Song, H. Q., et al. 2009, ApJ, 691, 1936
Cranmer, S. R. 2002, SSRv, 101, 229
Davies, J. A., Harrison, R. A., Perry, C. H., et al. 2012, ApJ, 750, 23
de Koning, C. A., Pizzo, V. J., & Biesecker, D. A. 2009, SoPh, 256, 167
DeForest, C. E., & Howard, T. A. 2015, ApJ, 804, 126
DeForest, C. E., Howard, T. A., & Tappin, S. J. 2011, ApJ, 738, 103
DeForest, C. E., Howard, T. A., Webb, D. F., & Davies, J. A. 2016, SpWea, 14, 32
Eyles, C. J., Harrison, R. A., Davis, C. J., et al. 2009, SoPh, 254, 387
Eyles, C. J., Simnett, G. M., Cooke, M. P., et al. 2003, SoPh, 217, 319
Feldman, U., Landi, E., & Schwadron, N. A. 2005, JGR, 110, A07109
Feng, X., Ma, X., & Xiang, C. 2015, JGR, 120, 10159
Feng, X., Yang, L., Xiang, C., et al. 2010, ApJ, 723, 300
Feng, X., Zhou, Y., & Wu, S. T. 2007, ApJ, 655, 1110
Gosling, J. T. 1996, ARA&A, 34, 35
Gosling, J. T., Bame, S. J., McComas, D. J., et al. 1993, GeoRL, 20, 2789
Gosling, J. T., & Pizzo, V. J. 1999, SSRv, 89, 21
Harrison, R. A., Davies, J. A., Möstl, C., et al. 2012, ApJ, 750, 45
Harrison, R. A., Davis, C. J., & Eyles, C. J. 2005, AdSpR, 36, 1512
Harrison, R. A., Davis, C. J., Eyles, C. J., et al. 2008, SoPh, 247, 171
Holzer, T. E. 1989, ARA&A, 27, 199
Howard, R. A., Moses, J. D., Vourlidas, A., et al. 2008, SSRv, 136, 67
Howard, T. A., & DeForest, C. E. 2012, ApJ, 752, 130
Howard, T. A., & Tappin, S. J. 2009, SSRv, 147, 31
Hundhausen, A. J. 1972, Coronal Expansion and Solar Wind, Physics and Chemistry in Space 5 (1st ed.; Berlin: Springer)
Jackson, B., Buffington, A., Hick, P., Bisi, M., & Clover, J. 2010, SoPh, 265, 257
Jian, L., Russell, C. T., Luhmann, J. G., & Skoug, R. M. 2006, SoPh, 239, 337
Kaiser, M. L., Kucera, T. A., Davila, J. M., et al. 2008, SSRv, 136, 5
Kuznetsov, V. D., Zelenyi, L. M., Zimovets, I. V., et al. 2016, Ge&Ae, 56, 781
Lee, M. A. 2000, JGR, 105, 10491
Leinert, C., & Pitz, E. 1989, A&A, 210, 399
Leinert, C., Pitz, E., Link, H., & Salm, N. 1981, Space Science Instrummentation, 5, 257
Li, B., Li, X., Hu, Y.-Q., & Habbal, S. R. 2004, JGR, 109, A07103
Liewer, P. C., Ayon, J., Alexander, D., et al. 2008, in NASA Space Science Vision Missions, Vol. 224, ed. M. S. Allen (Reston, VA: American Institute of Aeronautics and Astronautics), 1
Liu, Y., Davies, J. A., Luhmann, J. G., et al. 2010, ApJL, 710, L82
Liu, Y. D., Hu, H., Wang, C., et al. 2016, ApJS, 222, 23
Lugaz, N., Hernandez-Charpak, J. N., Roussev, I. I., et al. 2010, ApJ, 715, 493
Marsden, R. G., & Wenzel, K. P. 1981, Plasma Astrophys., 164, 51
McComas, D. J., Barraclough, B. L., Funsten, H. O., et al. 2000, JGR, 105, 10419
Moran, T. G., & Davila, J. M. 2004, Sci, 305, 66
Möstl, C., Rollett, T., Lugaz, N., et al. 2011, ApJ, 741, 34
Muller, D., Marsden, R. G., St, Cyr, O. C., & Gilbert, H. R. 2013, SoPh, 285, 25
Neugebauer, M., & Snyder, C. W. 1966, JGR, 71, 4469
Neugebauer, M., & Snyder, C. W. 1967, JGR, 72, 1823
Parker, E. N. 1958, ApJ, 128, 664
Pizzo, V. J., & Biesecker, D. A. 2004, GeoRL, 31, L21802
Plotnikov, I., Rouillard, A. P., Davies, J. A., et al. 2016, SoPh, 291, 1853
Rouillard, A. P., Davies, J. A., Forsyth, R. J., et al. 2008, GeoRL, 35, L10110
Rouillard, A. P., Savani, N. P., Davies, J. A., et al. 2009, SoPh, 256, 307
Schrijver, C. J., Kauristie, K., Aylward, A. D., et al. 2015, AdSpR, 55, 2745
Schwadron, N. A., Connick, D. E., & Smith, C. 2010, ApJL, 722, L132
Sheeley, N. R. J., Herbst, A. D., Palatchi, C. A., et al. 2008, ApJ, 674, 109
Smith, E. J., Marsden, R. G., & Page, D. E. 1995, Sci, 268, 1005
Suess, S. T. 1990, RvGeo, 28, 97
Tappin, S. J., & Howard, T. A. 2009, ApJ, 702, 862
Vourlidas, A., Howard, R. A., Plunkett, S. P., et al. 2016, SSRv, 204, 83
Wang, Y.-M., & Sheeley, N. R., Jr. 1990, ApJ, 355, 726
Wang, Y.-M., Sheeley, N. R., Jr., Walters, J. H., et al. 1998, ApJL, 498, L165
Wenzel, K. P., Marsden, R. G., Page, D. E., & Smith, E. J. 1992, A&AS, 92, 207
Wood, B. E., Howard, R. A., Thernisien, A., & Socker, D. G. 2010, ApJL, 708, L89
Wu, J., Sun, W. Y., Zheng, J. H., et al. 2011, AdSpR, 48, 943
Xiong, M., Davies, J. A., Bisi, M. M., et al. 2013a, SoPh, 285, 369
Xiong, M., Davies, J. A., Feng, X., et al. 2013b, ApJ, 777, 32
Xiong, M., Liu, Y., Liu, H., et al. 2016, ChJSS, 36, 245
Yang, L. P., Feng, X. S., Xiang, C. Q., et al. 2012, JGR, 117, A08110
Zhao, X. P., Hoeksema, J. T., & Scherrer, P. H. 2005, JGR, 110, A10101